Research of Low-cost Air Quality Monitoring Models with Different Machine Learning Algorithms

Gang Wang[1, 2, 3], Chunlai Yu[1, 3], Kai Guo[2], Haisong Guo[1, 3], Yibo Wang[2]

[1]Huanghe Science and Technology College, Zhengzhou 450063, China

[2]Hanwei Electronics Group Corporation, Zhengzhou 450001, China

[3]Zhengzhou Key Laboratory of Intelligent Measurement Techniques and Applications, Zhengzhou, 450063, China

Correspondence to: Gang Wang (wywanggang163@163.com)

Abstract. To improve the performance of the calibration model for the air quality monitoring, a low-cost multi-parameter air quality monitoring system (LCS) based on different machine learning algorithms is proposed. The LCS can measure particulate matter ($PM_{2.5}$ and PM_{10}) and gas pollutants (SO_2, NO_2, CO and O_3) simultaneously. The multi-input multi-output (MIMO) prediction model is developed based on the original signals of the sensors, ambient temperature (T) and relative humidity (RH), and the measurements of the reference instrumentations. The performance of the different algorithms (RF, MLR, KNN, BP, GA-BP) with parameters such as determination coefficient R^2, Root Mean Square Error (RMSE), and mean absolute error (MAE) are compared and discussed. Using these methods, the R^2 of the algorithms (RF, MLR, KNN, BP, GA-BP) for the PM is in the range 0.68 - 0.99; the RMSE values of $PM_{2.5}$ and PM_{10} are within 2.36 - 18.68 μgm^{-3} and 4.55 – 45.05 μgm^{-3}, respectively; the MAE values of $PM_{2.5}$ and PM_{10} are within 1.44 - 12.80 μgm^{-3} and 3.21- 23.20 μgm^{-3}, respectively. The R^2 of the algorithms (RF, MLR, KNN, BP, GA-BP) for the gas pollutants (O_3, CO and NO_2) is within 0.70 - 0.99; the RMSE values for these pollutants are 4.05 - 17.79 μgm^{-3}, 0.02 - 0.18 mgm^{-3}, 2.88 - 14.54 μgm^{-3}, respectively; the MAE values for these pollutants are 2.76 - 13.46 μgm^{-3}, 0.02 - 0.19 mgm^{-3}, 1.84 - 11.08 μgm^{-3}, respectively. The R^2 of the algorithms (RF, KNN, BP, GA-BP, except for MLR) for SO_2 is within 0.27 - 0.97, the RMSE value is in the range 0.64 -5.37 μgm^{-3}, and the MAE value is in the range 0.39 - 4.24 μgm^{-3}. These measurements are consistent with the national environmental protection standard requirement of China, and the LCS based on the machine learning algorithms can be used to predict the concentrations of PM and gas pollution.

1 Introduction

The development along with increased population and urbanization brings disadvantages, such as decreasing air quality and impact on public and individual health(Khreis et al., 2022; Manisalidis et al., 2020; Singh et al., 2021). Among the atmospheric pollutants, the primary pollutant is fine particulate matter, which affects the respiratory system and cardiac activity of humans. The secondary pollutants are SO_2, CO, NO_x, and O_3, which also induce disease or chronic poisoning. To improve the understanding of air pollution exposure and predict future air quality trends(Zimmerman et al., 2018), air quality assessment and forecasting are the essentials. The conventional air quality monitoring instrumentations are high cost, which has limited the spatial coverage of the monitoring stations(Zimmerman et al., 2018). The development and applications of the low-cost commercially available sensor-based air quality monitoring system (LCS) would considerably reduce both installation and maintenance costs(Spinelle et al., 2017). The larger spatial density of the air quality grid monitoring network becomes possible, which would play an important role in monitoring pollution trend, locating of pollution source, supporting environmental management(Zhao et al., 2019) and support better epidemiological models(Khreis et al., 2022; Zimmerman et al., 2018). These demands promote the LCS growing gradually(Cui et al., 2021; Wang et al., 2016).

The LCS typically utilizes the electrochemical or light scattering sensors for gas-phase or particulate pollutants measurement, such as sulfur dioxide (SO_2), nitrogen oxide (NO_2), carbon monoxide (CO), ozone (O_3) and particulate matters (PM). These electrochemical sensors have intrinsic problems, such as temperature or humidity impacts, and gaseous cross-sensitivities (Spinelle et al., 2015, 2017; Wan et al., 2016; Zimmerman et al., 2018). For example, limited by the poor selection performance, the NO_2 electrochemical sensor also undergo redox reactions in the presence of O_3 gaseous pollutants. The diffusion coefficient of the electrochemical sensor can be affected by temperature and relative humidity(Hitchman et al., 1997; Masson et al., 2015). The reagent of the electrochemical sensor is consumed over time, which affects the stability of the sensor. These features of the sensors have historically been poorly addressed by laboratory calibrations, limiting the utility for air quality monitoring(Zimmerman et al., 2018).

The de-convolving of cross-sensitivity effect and stability on sensor performance is complex(Zimmerman et al., 2018). The linear or multivariate linear calibration models (Alexopoulos, 2010; Khreis et al., 2022; Zoest et al., 2019) have been developed. However the performance is poor on ambient data(Khreis et al., 2022). The accurate and precise calibration models for the low cost sensors are particularly critical to the success of dense sensor networks, as poor signal to noise ratios and cross-sensitivities hamper their ability to distinguish the pollutant concentrations. There has been increasing interest in multifarious algorithms for low-cost sensor calibration, and lots of studies using multi-input multi-output models(Alexopoulos, 2010) and neural networks(Spinelle et al., 2015) have been published. The artificial neural network (ANN) calibration model has the intelligence to process nonlinear data (Amuthadevi et al., 2021; Janabi et al., 2021), which has been used in calibration models for measuring ozone or nitrogen oxide(Esposito et al., 2016; Spinelle et al., 2015). For example, the ANN calibration model was used to calibrate O_3 and the uncertainty could meet the European data quality objectives; however, meeting these objectives for NO_2 remained a challenge(Spinelle et al., 2015). Dynamic neural network calibrations of NO_2 sensors were demonstrated with the mean absolute error less than 2 ppb; however, the performance for O_3 was not same(Esposito et al., 2016). High-dimensional multi-response model was used to calibrate CO, NO, NO2, and O3, with the 5 min average RMSE values of 39.2, 4.52, 4.56, and 9.71, respectively(Cross et al., 2017). Random-forest-based machine learning algorithm was used to improve the calibration strategies of low-cost sensors, with the mean absolute error values 38 ppb for CO, 10 ppm for CO_2, 3.5 ppb for NO_2, and 3.4 ppb for O_3, respectively(Zimmerman et al., 2018). Furthermore, multiple linear regression(Ionascu et al., 2021) based temperature and humidity correction and ANN based calibration shown the potential for significant further improvement for leave one out cross validation(Ali et al., 2021). With the 16 days process, the combined supervision calibration model was used to improve the R^2 of SO_2, NO_2 and O_3 by 75.8%, 38.6% and 4.7% to 0.58, 0.61, and 0.90, respectively(Cui et al., 2021). An integrated genetic programming dynamic neural network model was used to accurately estimate the carbon monoxide and nitrogen dioxide pollutant concentrations from the multi-sensor measurement data(Davut et al., 2022). A predictive model using multilayer perceptron, support vector regression, and linear regression was developed to analyze the CO_2 and particulate matter of in-vehicle, with the R^2 of 0.9981(Chew et al., 2021). The CNN, LSTM-CNN, and CNN-LSTM models were used to improve the prediction performance of the ozone by 3.58%, 1.68%, and 3.37%, respectively(Reza et al., 2023). However, these calibrations have only been tested utilizing fewer models with a short measurement period and small number of sensor matrix, each containing one sensor per pollutant (Cross et al., 2017; Esposito et al., 2016; Spinelle et al., 2015), not have been utilized to evaluate and predict the concentration values of multi pollutants simultaneously, such as $PM_{2.5}$, PM_{10}, SO_2, NO_2, CO and O_3.

The random-forest (RF)(Breiman, 2001; Liu et al., 2012), multivariate linear regression (MLR)(Alexopoulos, 2010), K Nearest Neighbor (KNN)(Zhao et al., 2021), BP neural network(Xu et al., 2021), and genetic-algorithm-back-propagation neural (GA-BP) network(Ning et al., 2019; Wang et al., 2019) are five commonly used machine learning algorithms with different characteristics. With the strong nonlinear mapping ability and adaptive ability, the RF, BP, and GA-BP are suitable for processing complex, high-

1 dimensional, and nonlinear data with high prediction accuracy, such as the air quality monitoring. With the purpose to quantify the

2 degree of influence of the independent variable, the MLR is suitable for evaluating the influence of multiple independent variables

3 on the dependent variable, such as the cross-sensitivity effect between different factors. The KNN is also a widely common

4 algorithm to compare with RF, BP, GA-BP and MLR.

5 In this work, the LCS is developed to measure $PM_{2.5}$, PM_{10}, SO_2, NO_2, CO and O_3 simultaneously, and the performances of the

6 calibration strategies based on the five machine learning algorithms are contrasted. Taking the original electronic signals of the

7 sensors as input and measurements obtained by the reference instrumentations as output, five calibration strategies are applied and

8 contrasted. The measurement is implemented in the real-world conditions almost a 12-month period (1 March 2021 and 28

9 February 2022) spanning multiple seasons and a wide range of meteorological conditions to ensure calibration model robustness.

10 The performance of the different algorithms with the parameters, such as determination coefficient (R^2), root mean square error

11 (RMSE) (Janabi et al., 2021), and mean absolute error (MAE), are compared and discussed. The rest of this paper is organized as

12 follows. The measurement setup is described in section 2. The principles of the calibration strategies are presented in section 3.

13 The results and discussion are shown in section 4. The conclusion and discussion are drawn in section 5.

14 **2 Measurement setup**

15 This section describes the measurement site and data collection, schematic block of the LCS, and the reference instrumentation.

16 The low-cost here is defined as below 150 dollars per pollutant, commercial availability and low maintenance. The sensors typically

17 utilize electro-chemical signal and scattering light intensity for gas-phase pollutants (SO_2, NO_2, CO and O_3) and particle pollutants

18 ($PM_{2.5}$, PM_{10}) measurement.

19 **2.1 Measurement site and data collection**

20
21 **Figure 1 Location of the air quality monitoring station during the measurement period**
22

23 Measurements for gas-phase pollutants and particle pollutants were made continuously between 1 March 2021 and 28 February

24 2022, which were used as the start and end dates for the analyses. The location, shown in Figure 1, was 30 Yaochang Streat,

25 Zhongyuan District, Zhengzhou City, Henan Province of China. There was an independent reference monitoring system for $PM_{2.5}$,

26 PM_{10}, CO, SO_2, NO_2 and O_3 measurement. The LCS was mounted at a consistent height with the reference monitoring system.

27 The time taken for one set of data collection was one minute and repeated 4 times. The outlier of the 4 sets of data was eliminated

28 by using the Dixon principle. The remained data was used to get the mean values for each experiment. The values of the LCS and

1   reference instruments were separately logged to the server with the interval of 5 minutes. During the measurement period, the

2   ranges of the ambient temperature and relative humidity separately were minus 5°C to plus 50°C and 10% to 98%.

3   **2.2 Schematic block of LCS**

(a)   (b)
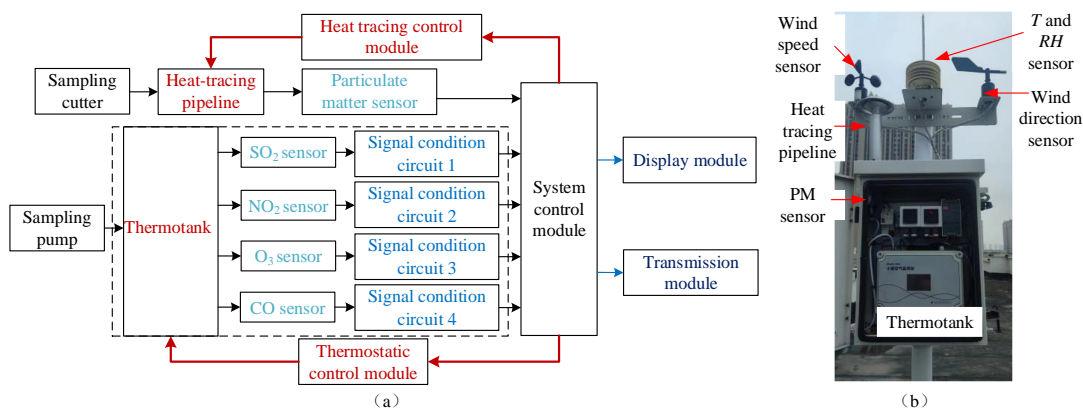
5   **Figure 2. Schematic block and site photo of the LCS. The left panel (a) is the schematic block of the LCS. The system control module can**
6   **ensure the temperature stability of the heat tracing pipeline and thermo-tank through the heat tracing control module and thermostatic**
7   **control module, respectively. The sampling cutter is used to filter particles larger than 10 µm. The sampling pump is utilized to deliver**
8   **ambient air to the surface of the sensors. The right panel (b) is the site photo of the LCS.**

10   In this study, the LCS is developed by Hanwei Electronics Group Corporation, and its schematic block diagram is shown in Figure 2.

11   The LCS uses the commercially available particulate matter sensor (PM3006, Cubic sensor and Instrument Co., China) and

12   electrochemical SO_2, NO_2, O_3, CO sensors (B4, Alphasense, UK), respectively. The particulate matter sensor device is the laser

13   diode (LD) based particle sensor, using a spectrophotometer to measure the particle scattering light intensity. The PM sensor device

14   (PM3006) can measure size dependent $PM_{2.5}$ and PM_{10} concentration of the particles in the size range of 0.3 to 10 µm. The gas

15   pollution ($SO_2\backslash NO_2\backslash O_3\backslash CO$) sensor used are with 4 electrodes (i.e. reference, worker, counter and auxiliary electrodes), where the

16   auxiliary electrode is not exposed to the target analyte to account for changes in the sensor baseline signal under different

17   meteorological conditions(Mead et al., 2013).

18   The electrochemical sensor outputs are measured using electronic circuitry designed by Hanwei and optimized for signal stability.

19   The circuitry is developed with custom electronics to drive the device, multiple stages of filtering circuitry for specific noise

20   signatures, and an analog-to-digital converter for measurement of the conditioned signal.

21   Due to the redox reaction on the anode and the cathode of the electrochemical sensor, the movement of charge between the

22   electrodes produces a current proportional to the analyte reaction rate, which can be used to determine the analyte

23   concentration(Mead et al., 2013) and the sensor whether working effectively.

24   Before installed into the LCS, calibrated with the different models and used in real-world conditions, the performance of the sensors

25   should be checked in laboratory. The linearity of the gas sensors was tested under steadily increased concentration, which was

26   from 0 - 5 mgm^{-3} for CO sensor, 0 - 0.2 mgm^{-3} for NO_2, 0 - 1.1 mgm^{-3} for O_3 and 0 - 1.4 mgm^{-3} for SO_2 with five more test points,

27   shown in Figure 3. Since the units of outputs of the reference instruments and the sensors were different, the slope was not expected

28   to be 1(Cui et al., 2021). As shown in Figure 3, the R^2 for the gas sensors are more than 0.93, which indicated that these gas sensors

29   have good linear responses before calibration, and verified the sensor working properly and effectively and could be applied to the

30   LCS.
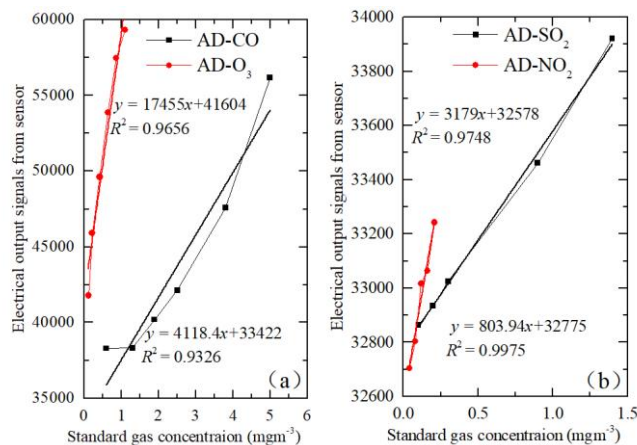
2 **Figure 3. Linearity of gas sensors before calibration. Electrical output signals versus single standard gas concentration is tested in**
3 **laboratory condition. The left panel (a) and right panel (b) represent the proportional relations between CO and O₃ sensors, SO₂ and**
4 **NO₂ sensors, respectively. The duration of each measurement is about 30 minutes.**

6 However, even with an auxiliary electrode, electrochemical sensors may insufficiently account for the impacts of temperature and
7 relative humidity. With the standard gases through the test chamber and the concentrations stabilized at 27 ppb for SO_2, 3.9 ppb
8 for NO_2, 13 ppb for O_3, and 1.22 ppm for CO, the output voltages of the four types of gaseous sensors are nonlinearly fluctuated
9 with the linearly increasing temperature and the relative humidity (RH)(Cui et al., 2021). With the purpose to eliminate the
10 influence of the external environment on the sensor as much as possible, the particles flow through a sampling cutter and heat-
11 tracing pipeline to the particulate matter sensor, and the gaseous pollutants are pumped to the electrochemical sensors, which are
12 secured in a thermo-tank. The temperature values of the heat-tracing pipeline and thermo-tank can be maintained at 60 °C±2 °C to
13 reduce the influence of relative humidity and 25 °C ±2 °C(Wei et al., 2018) to keep the sensor operating at a stable temperature,
14 respectively.
15 The measurement results of particulate matter sensor and gas pollution sensors, transmitted to the system control module through
16 the data buses, are directly displayed on the local display module and wirelessly transmitted to the corresponding online server
17 through the transmission module. As the uni-variate linear models does not in-corporate any cross-sensitivities to other pollutants
18 or any nonlinearities in the response, we attempt to using the sensor electronic results as the input and the reference measurements
19 as the output, to build multi-dimensional multi-response prediction models to de-convolve the effects of cross-sensitivity and
20 stability on sensor performance utilizing MLR, RF, KNN, BP and GA-BP calibration models.

21 **2.3 Reference instrumentation**

22 In order to reduce the adsorption effect on particle matter and gaseous pollutants, the reference measurements are made on ambient
23 air continuously drawn through Teflon fluorinated ethylene propylene (FEP)(Wei et al., 2018) tubing with a six-port stainless steel
24 manifold for flow distribution to the gas analyzers and particulate monitors(Mead et al., 2013). It should be pointed out that the
25 LCS was mounted at a consistent height with the reference monitoring system during the measurement period.
26 The reference ambient particulate monitor 5014*i*, which uses beta attenuation of the ambient particulate deposited onto a filter tape,
27 is applied to measure the mass concentration of suspended and refined particulates. The reference NO-NO₂-NOₓ monitor 42*i*, using
28 the linear proportional of the chemi-luminescence reaction of NO and O_3 after NO_2 transformed into NO, is utilized to measure the
29 NO_2 concentration. The SO_2 reference analyzer is 43*i* using the ultraviolet light (which is emitted as the excited SO_2 molecules
30 decay to lower energy states) intensity proportional to the SO_2 concentration. The CO reference monitor is 48*i* utilizing the principle
31 that CO absorbs infrared radiation at a wavelength of 4.6 μm and the infrared absorption can be transformed to be proportional to

1 the CO concentration. The 49i O$_3$ analyzer operates on the principle that O$_3$ molecules absorb UV light at a wavelength of 254 nm,

2 and the absorption intensity of the UV light is directly related to the ozone concentration. All these reference monitors are produced

3 by Thermo Fisher Scientific Inc. The time interval for all reference measurements is 5 minutes. According to the technical

4 specifications for operation and quality control of ambient air quality continuous automated monitoring system for SO$_2$, NO$_2$, O$_3$

5 and CO of China(China, 2018), and the technical guide for automatic monitoring by beta ray method for particulate matter in

6 ambient air (PM$_{10}$ and PM$_{2.5}$) (China, 2020), the reference gas and particulate analyzers are checked and calibrated weekly and

7 monthly, respectively.

8 **3 Principles**

9 This section describes the principles of the calibration methods, such as MLR, BP, GA-BP, KNN and RF, and the metrics for

10 performance evaluation. The calibration models are constructed with the sensors (i.e., PM$_{2.5}$, PM$_{10}$, CO, SO$_2$, NO$_2$ and O$_3$ sensors.)

11 electronic results as the input and the reference measurements as the output.

12 **3.1 Calibration methods**

13 **3.1.1 Multiple linear regression model**

14 After the data collected by the LCS, the raw data should be preprocessed. The PM3006 particulate matter sensor can output six

15 kinds of particle range (i.e., >0.3μm, >0.5μm, >1.0μm, >2.5μm, >5.0μm and >10μm, respectively). By subtracting the six particle

16 range values in turn, the individual particle counters are obtained, and expressed as $x_{0.5}$, $x_{1.0}$, $x_{2.5}$, $x_{5.0}$ and $x_{10.0}$, listed in Table 1, the

17 measured particle number concentration is converted to PM mass concentrations in the PM$_{2.5}$ and PM$_{10}$ size fractions.

19 **Table 1. Size range of the particulate matter sensor. The sensor can measure particles with the size range of 0.3~0.5 μm, 0.5~1.0 μm,**
20 **1.0~2.5 μm, 2.5~5.0 μm and 5.0~10 μm, simultaneously. The corresponding particle counters are expressed as $x_{0.5}$, $x_{1.0}$, $x_{2.5}$, $x_{5.0}$ and $x_{10.0}$,**
21 **respectively.**

Range (μm)	0.3~0.5	0.5~1.0	1.0~2.5	2.5~5.0	5.0~10.0
Particle counter	$x_{0.5}$	$x_{1.0}$	$x_{2.5}$	$x_{5.0}$	$x_{10.0}$

22
23 Taking the particle counters, listed in Table 1, as input and the concentrations $Y_{pm2.5}$ and Y_{pm10} of PM$_{2.5}$ and PM$_{10}$ measured by

24 5014i as output, the multivariate linear regression (MLR) models(Alexopoulos, 2010; Zoest et al., 2019) is built. Due to the

25 previously established influence of ambient temperature (T) and relative humidity (RH) on sensor response(Masson et al., 2015;

26 Wan et al., 2016), the particle counter terms are pretreated and individual from each other. The multi-input one-response

27 preprocessing and prediction models can be written as Eq. (1) to obtain the concentrations $Y_{pm2.5}$.

28 $Y_{pm2.5}=w_{1\_pm2.5} \cdot x_{0.5} + w_{2\_pm2.5} \cdot x_{1.0} + w_{3\_pm2.5} \cdot x_{2.5} + w_{4\_pm2.5} \cdot T + w_{5\_pm2.5} \cdot RH + b_{pm2.5}$, (1)

29 Where $W_{pm2.5}= [w_{1\_pm2.5}, w_{2\_pm2.5}, w_{3\_pm2.5}, w_{4\_pm2.5}, w_{5\_pm2.5}]$ is the corresponding weight coefficients; the $X_{pm2.5} = [x_{0.5}, x_{1.0}, x_{2.5}, T,$

30 $RH]$ represents the individual particle counters, the temperature sensor and humidity sensor; the $b_{pm2.5}$ is the intercept values of the

31 model.

32 To obtain the concentration Y_{pm10}, the multi-input one-response preprocessing and prediction models can be written as Eq. (2).

33 $Y_{pm10}=w_{1\_pm10} \cdot x_{0.5} + w_{2\_pm10} \cdot x_{1.0} + w_{3\_pm10} \cdot x_{2.5} + w_{4\_pm10} \cdot x_{5.0} + w_{5\_pm10} \cdot x_{10.0} + w_{6\_pm10} \cdot T + w_{7\_pm10} \cdot RH + b_{pm10}$, (2)

34 Where $W_{pm10} = [w_{1\_pm10}, w_{2\_pm10}, w_{3\_pm10}, w_{4\_pm10}, w_{5\_pm10}, w_{6\_pm10}, w_{7\_pm10}]$ is the corresponding weight coefficients; the $X_{pm10} =$

35 $[x_{0.5}, x_{1.0}, x_{2.5}, x_{5.0}, x_{10.0}, T, RH]$ represents the individual particle counters, the temperature sensor and humidity sensor; the b_{pm10} is

36 the intercept values of the model.

1   Due to the poor selection performance and cross interference of the electro-chemical sensors response, the output values from each

2   sensor using net sensor response to the target analyte, such as O_3, NO_2, SO_2, concentration measured by the inference monitor are

3   used to build the MLR model. The CO gaseous pollution is also one of the criteria pollutants, which is must to be measured in

4   China. Thus, the multi-dimensional multi-response preprocessing and prediction model for the 4 gas pollutions, T and RH can be

5   written as Eq. (3).

$$\begin{cases} Y_{SO_2}= w_{11}\cdot x_{SO_2}+w_{12}\cdot x_{NO_2}+w_{13}\cdot x_{CO}+w_{14}\cdot x_{O_3}+w_{15}\cdot T+w_{16}\cdot RH+b_{SO_2} \\ Y_{NO_2}= w_{21}\cdot x_{SO_2}+w_{22}\cdot x_{NO_2}+w_{23}\cdot x_{CO}+w_{24}\cdot x_{O_3}+w_{25}\cdot T+w_{26}\cdot RH+b_{NO_2} \\ Y_{CO}= w_{31}\cdot x_{SO_2}+w_{32}\cdot x_{NO_2}+w_{33}\cdot x_{CO}+w_{34}\cdot x_{O_3}+w_{35}\cdot T+w_{36}\cdot RH+b_{CO} \\ Y_{O_3}= w_{41}\cdot x_{SO_2}+w_{42}\cdot x_{NO_2}+w_{43}\cdot x_{CO}+w_{44}\cdot x_{O_3}+w_{45}\cdot T+w_{46}\cdot RH+b_{O_3} \end{cases},$$
(3)

7   The equation (3) can be simplified as,

8    $Y_{[SO_2, NO_2, CO, O_3]}=W_{gas}\cdot X_{gas} + B_{gas}$,   (4)

9   Where $W_{gas}=\begin{bmatrix} w_{11} & w_{12} & w_{13} & w_{14} & w_{15} & w_{16} \\ w_{21} & w_{22} & w_{23} & w_{24} & w_{25} & w_{26} \\ w_{31} & w_{32} & w_{33} & w_{34} & w_{35} & w_{36} \\ w_{41} & w_{42} & w_{43} & w_{44} & w_{45} & w_{46} \end{bmatrix}$ is the corresponding weight coefficient; the $X_{gas} =[x_{SO_2}, x_{NO_2}, x_{CO}, x_{O_3}, T,$

10    $RH]$ is the convertor output values of the sensors through the electronic circuitries; the $B_{gas} = [b_{SO_2}, b_{NO_2}, b_{CO}, b_{O_3}]$ is the

11   intercept value of the model.

12   Hereto, the multi MLR models for the gas sensor and PM sensor are separately developed. The training data is used to calculate

13   the model regression coefficient and intercept values, and the withheld testing data is utilized to evaluate the performance of the

14   model performance.

15   **3.1.2 BP neural network model**

16   The BP neural network algorithm is one of the most widely used ANN models. It is a multi-layer feed-forward network trained

17   through an error back propagation algorithm by constantly adjusting the weight and intercept of the network. The feed-forward

18   topological structure of the BP neural network model, shown in Figure 4, includes the input layer, hidden layer and output layer.

19   With the purpose to avoid the numerical problems caused by the extreme values of polarization, eliminate the misleading effects

20   for feature extraction and obtain the accurate estimation of pollutant concentrations(Janabi et al., 2021), the collected input sensor

21   date X_I and output date Y_O should be respectively normalized with min-max normalization to limit values in each dimension

22   between 0 and 1(Hande et al., 2021).
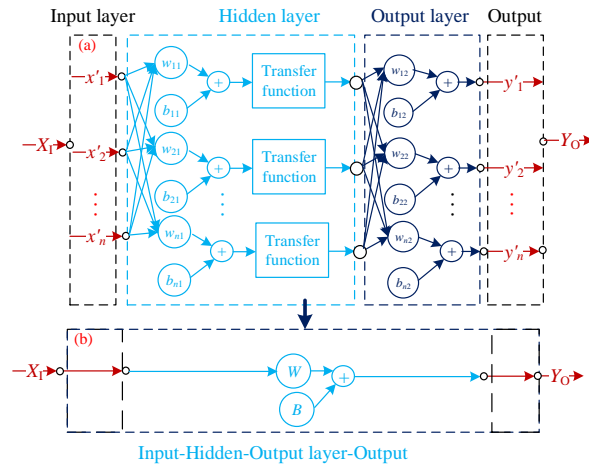
23
24   **Figure 4. Topological structure of BP neural network model. The up panel (a) is the feed-forward topological structure. The X_I and Y_O**
25   **are the input data and output data, respectively. The X'_i and Y'_i separately indicate the normalized items of X and Y. The w_{i1} and b_{i1}, w_{j2}**
26   **and b_{j2} separately represent the weight value and intercept value of the hidden layer and output layer. The down panel (b) is equivalent**

to panel (a) to simplify the formulas.

After the normalization process, the BP network can be established. To optimize the best parameters of the network, the number of hidden layer, the transfer functions of the layers, and the end conditions should be determined. If the parameters are inappropriate, the BP-model will be over trained or insufficient. In this study, a shallow structure with a single hidden layer is chosen, as extensive testing did not show any noticeable improvement in calibration performance with deeper structure consisting of multiple hidden layers(Ali et al., 2021). This also reduced the complexity and the training time.

3.1.3 Genetic algorithm-BP model

In the traditional BP neural network, the initial weights and thresholds are randomly generated. The results often fall into a local minimum rather than a global minimum, and would lead to the distortion of the prediction result. In addition, the convergence speed of the BP neural network is usually slow. To solve these problems, the genetic algorithm (GA) (Liang et al., 2018) with BP algorithm is also used to avoid the inherent defects of BP algorithm. The GA method is essentially a direct search method that does not rely on specific problems and gradient information. It follows the survival and elimination rule of biological evolution, generates the following hypotheses by mutating and reconstructing the best existed hypothesis and makes it possible to solve the problem(Ning et al., 2019). Generally, the GA is used to find an optimal initial weight and a threshold value for the model, so that the model could converge in the direction of minimum value(Wang et al., 2019). The GA-BP hybrid algorithm is used to reduce the time for the BP neural network to adjust the weight and threshold itself and achieve the goal of improving work efficiency.

3.1.4 K nearest neighbor model

The k nearest neighbor (KNN) is also one of the simplest method for classification as well as regression problem(Kumar, 2015; Zhao et al., 2021). The KNN is a supervised method that uses estimation based on values of neighbors, which can automatically adapt to the supervised learning problems with arbitrary Bayes decision boundaries(Zhao et al., 2021). From the supervisor dataset, the KNN solution utilizes the values of given dependent variable y_i to approximate the dependent variable y^*, which is close with respect to distance between their corresponding model parameters. For regression problem, the mean of the observed labels of k nearest neighbors of independent variable X is assigned to be the predicted label. In this study, the k is set to 10 with the performance having no obvious difference from other numbers.

3.1.5 Random forest model

The random forest (RF) model is used for solving regression or classification problems(Breiman, 2001; Liu et al., 2012). It works by constructing an ensemble of decision trees using a training data set; the mean value from that ensemble of decision trees is then used to predict the value for new input data(Zimmerman et al., 2018). With the purpose to establish a RF model, the maximum number of decision trees of the forest should be specified. Each tree is constructed using a bootstrapped random sample from the training data set. By considering a random subset of the possible explanatory variables with the strongest predictor of the response, the origin node of the decision tree can be split into sub-nodes. The node splitting process is repeated until a terminal node is reached. The terminal node can be specified using the maximum number of sub-nodes or the minimum number of data points in the node. To illustrate the method, consider building a random forest model for one LCS using a single decision tree and a subset of 20490 data points to build a calibration model, shown in Figure 5. The RF model can predict data with variable parameters within the training range. Therefore, a larger and more variable training data set should create a better final model. To avoid missing any spikes during the training window, a 5-fold cross-validation approach(Zimmerman et al., 2018) is also used to maximize

1 utilization of the training data set. This approach helps to minimize bias in training data selection when predicting new data and

2 ensures that every point in the training window is used to build the model.
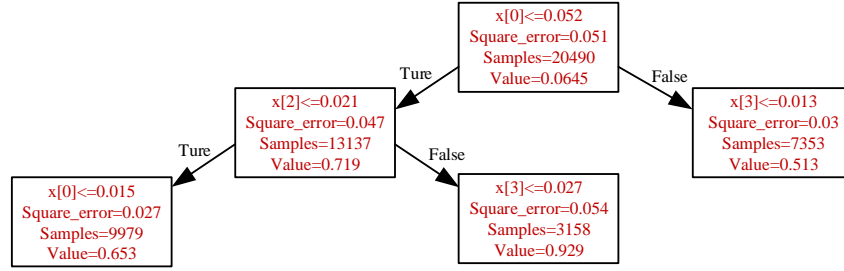
4 **Figure 5. Simplified illustration of the RF with a single decision tree and a subset. The $x[0]$, $x[2]$, $x[3]$ represent the CO, SO$_2$ and O$_3$**
5 **pollutants. At the first split, points with normalized CO sensor signal ≤0.052 are sent to a terminal node; the remaining points go to the**
6 **other splitting node. The Samples is the number of data points in each terminal node. The Value is the average in each terminal node.**

7 **3.2 Metrics for performance evaluation**

8 To quantitatively compare the performances of the five calibration models applied to the LCS, and balance the disadvantages of

9 the different metrics, the determination coefficient (R^2), root mean square error (RMSE) (Janabi et al., 2021), and mean absolute

10 error (MAE) are utilized. The R^2 reflects the fit degree between the model output data and the reference monitor measurement.

11 The measurement results should meet the requirements of environmental standards of China(Wan et al., 2016). The RMSE

12 measures how much error there is between the predicted values and the reference measurements, and is sensitive to extreme

13 values(Chai et al., 2014). The MAE is a good choice to evaluate the error when the distribution is not Gaussian (Reza et al., 2023).

14 The formulas for the evaluation metrics are presented as equations (5) - (7), respectively.

15 $$R^2 = 1 - [\sum_{i=1}^{n} (y_i - \hat{y}_i)^2] / [\sum_{i=1}^{n} (y_i - \bar{y}_i)^2],$$ (5)

16 $$\text{RMSE} = \sqrt{\frac{1}{n} \sum_{i=1}^{n} (y_i - \hat{y}_i)^2},$$ (6)

17 $$\text{MAE} = \frac{1}{n} \sum_{i=1}^{n} |y_i - \hat{y}_i|,$$ (7)

18 Where $\hat{y}_i$, y_i and $\bar{y}$ represent the ith model output data form the algorithm-based LCS system, the reference data from the reference

19 instrumentations, and the mean value of the reference instrumentations, respectively. The n is the number of the measurement data

20 in the dataset.

21 **4 Results and discussion**

22 Following the model building, the goodness of regression and root mean square error between the model output concentrations

23 and the reference monitor concentrations are evaluated for all calibration model approaches. The plots for the PM$_{2.5}$, PM$_{10}$, O$_3$, CO,

24 NO$_2$ and SO$_2$ illustrating the time series and goodness of fit of the models are provided in the Figure 6 - Figure 15. The R^2 and

25 RMSE values are listed in Table 2 - Table 9.

26 **4.1 Parameters of the model**

27 For the BP and GA-BP models, the parameters are the functions for the hidden layer and output layer, the type of the hidden layer,

28 the number of iteration times, and the number of the nerve units(Xu et al., 2021). The functions for the hidden layer and output

29 layer in this study respectively are the default tansig and the purelin functions. With the more complex type of the hidden layer

30 and less obvious improvement, the hidden layer is single type to achieve the goal of work efficiency.

31 To determine the best number of iteration times and nerve units, the measurement from the LCS and reference monitor between 1

1 March 2021 and 30 June 2021 is used. The number of iteration time is optimized using the mean squared error (MSE) between the

2 model value from the model and the reference monitor output value. The tendency of the MSE is shown in Figure 6. The training

3 is performed for 500 iterations. It is observed that the MSE decreases with the number of iteration time increasing, the rate of

4 decrease and the variation of the MSE is negligible beyond 100 iterations. More iterations incur higher computational cost for the

5 training and small performance improvement. There is also the risk of overtraining resulting in poor generalization capability.

6 Using this method, the same number of iteration times can be obtained with the different gas pollutants within 1 July 2021 and 31

7 October 2021, 1 November 2021 and 28 February 2022.
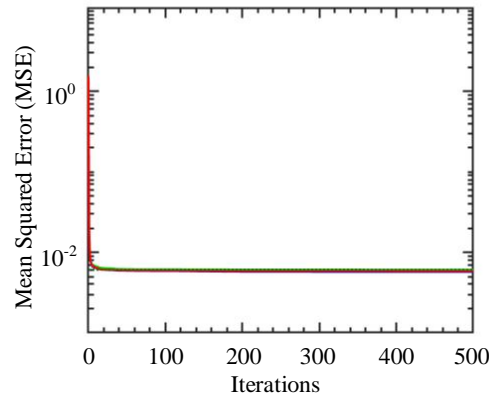
9 **Figure 6. The MSE with the number of iterations.**
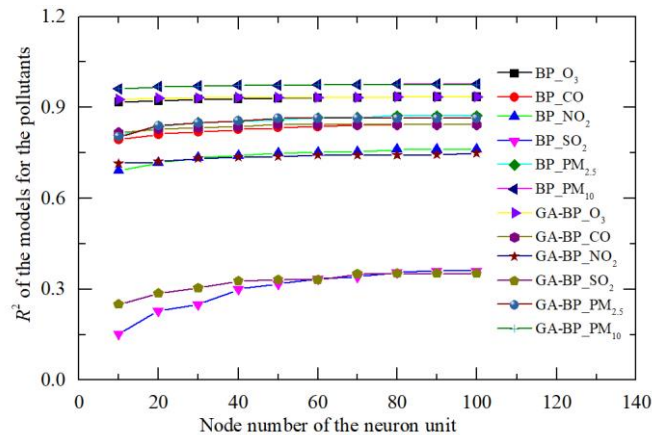
11 **Figure 7. The R^2 with different node number of the neuron for the pollutants.**

12 The node number of the nerve units is determined by the contrast results of determination coefficient R^2 for different gas and PM

13 pollutants within 1 March 2021 and 30 June 2021. The results are shown in Figure 7. The R^2 is improved as the number of nerve

14 units increasing. The rate of increase and the variation of R^2 is negligible beyond 70 units. More units incur higher computational

15 cost and time for the training and small performance improvement. Using this method, the same number of the nerve units can be

16 obtained with the different gas pollutants within 1 July 2021 and 31 October 2021, 1 November 2021 and 28 February 2022.

17 For the RF model, the number of trees is determined by using grid search method, which will search the optimal hyper-parameter

18 by traversing a given hyper-parameter combination (Zhu et al., 2022). A total of 11 kinds of tree numbers are set between 2 and

19 22. By using grid search to traverse these 11 kinds of tree numbers to obtain different R^2. For instance, the R^2 for different gas

20 pollutants within 1 March 2021 and 30 June 2021 are shown in Figure 8. The R^2 is improved as the number of trees increasing.

21 The rate of increase and the variation of R^2 is negligible beyond 20. The terminal node is specified using a maximum number of

22 sub-node points per node. The R^2 is also improved as the number of sub-node increasing under the same tree number. The rate of

23 increase and the variation of R^2 is negligible beyond 100. More number of the tree or the sub-node incur higher computational cost

1 and time for the training and small performance improvement. Using this method, the same number of trees can be obtained with

2 the different gas pollutants within 1 July 2021 and 31 October 2021, 1 November 2021 and 28 February 2022.
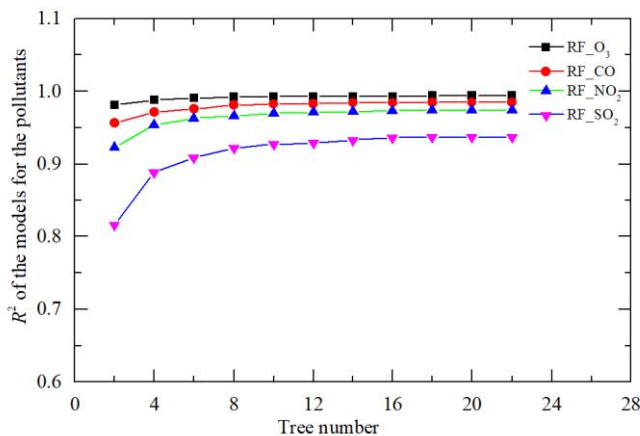
4 **Figure 8. The R^2 with different tree number of the RF model for the pollutants.**

5 **4.2 Measurement results of PM**

6 With the purpose of avoiding over-fit in the five models, the random partition parameters of train ratio and test ratio are 80% and

7 20%, respectively. To ensure the robustness of the model evaluation, the 5-fold cross validation is also conducted. The dataset is

8 divided into 5 mutually exclusive subsets with same size, where the 4 subsets are randomly selected as the training set each time,

9 and the remaining 1 subset is used as the test set. After completing each round of validation, 4 copies are selected again to train

10 the model and the remaining 1 copy is used for validation. After several rounds (less than 5), the loss function is selected to evaluate

11 the optimal model and parameters (Mahesh et al., 2023; Zimmerman et al., 2018).

12 With the results from 1 March 2021 to 28 February 2022 and according the trend of the ambient temperature, the whole data is

13 divided into three segments. The three segments (I, II, and III) separately are within 1 March 2021 and 30 June 2021 with the size

14 of 32481, 1 July 2021 and 31 October 2021 with the size of 31287, 1 November 2021 and 28 February 2022 with the size of 32053,

15 respectively.

16 During the measurement period, the ranges of the ambient temperature and relative humidity separately were minus 5°C to plus

17 50°C and 10% to 98%., shown in Figure 9. The ambient temperature raised, dropped and fluctuated separately within 1 March

18 2021 and 30 June 2021, 1 July 2021 and 31 October 2021, 1 November 2021 and 28 February 2022. The time series data and

19 regressions of five modes for PM from reference monitor and LCS calibration output are shown in Figure 10 and Figure 11.
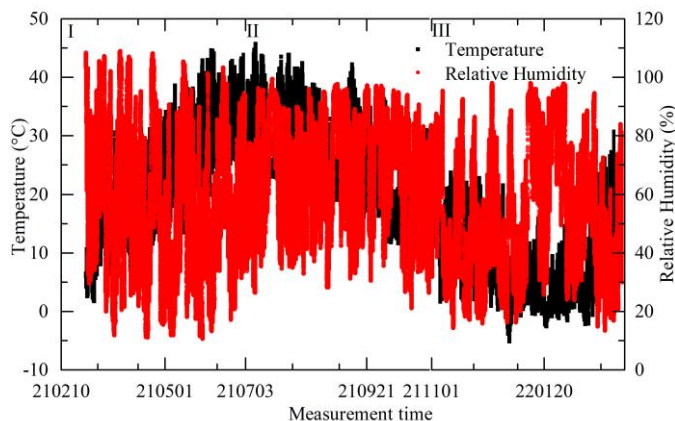
20
21 **Figure 9 Temperature/relative humidity ranges during the measurement period.**
22
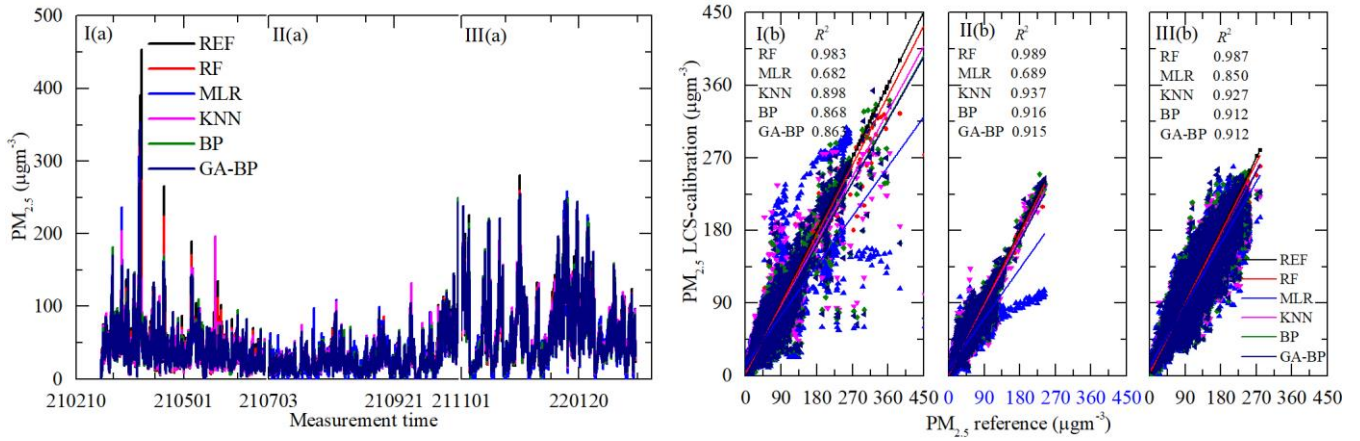
2 **Figure 10. Time series and regressions comparing the reference monitor PM$_{2.5}$ data (black) to five calibration model PM$_{2.5}$ results. Where**
3 **red, blue, magenta, olive and navy represent RF, MLR, KNN, BP, GA-BP, respectively. The left panel (a) shows the whole time series**
4 **data of the measurement period. The right panel (b) shows the regressions of the five calibration models.**
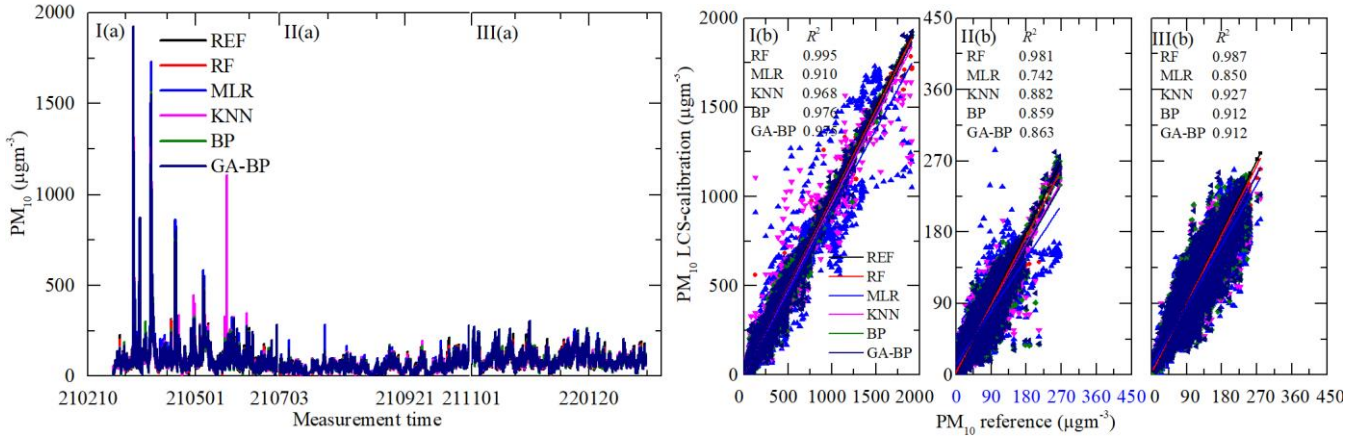
7 **Figure 11. Time series and regressions comparing the reference monitor PM$_{10}$ data (black) to five calibration model PM$_{10}$ results. Where**
8 **red, blue, magenta, olive and navy represent RF, MLR, KNN, BP, GA-BP, respectively. The left panel (a) shows the whole time series**
9 **data of the measurement period. The right panel (b) shows the regressions of the five calibration models.**

11 As shown in Figure 10(a) and Figure 11(a), the general tendency of the data fluctuation between the reference monitor and the RF,

12 MLR, KNN, BP, GA-BP based algorithm of the LCS are consistent with each other. The best performance is RF model, the next

13 are KNN, BP and GA-BP, the worst is MLR.

14 The R^2 between the reference data and the five model data are also shown in Figure 10(b) and Figure 11(b), and listed in Table 2.

15 The R^2 of RF for the PM is better than 0.98. The R^2 of MLR for the PM is less than 0.91, and even less than 0.7. The R^2 of the

16 other three model are within 0.86 and 0.98.

18 **Table 2. Performance of different calibration models for the PM$_{2.5}$ and PM$_{10}$ against reference monitor. The determination coefficient R^2**
19 **(higher is better, maximum of 1) of different calibration models (RF, MLR, KNN, BP, GA-BP) versus reference monitor.**

R^2 Model	PM$_{2.5}$			PM$_{10}$		
	I	II	III	I	II	III
RF	**0.983**	**0.989**	**0.987**	**0.995**	**0.981**	**0.987**
MLR	0.682	0.689	0.850	0.910	0.742	0.850
KNN	0.898	0.937	0.927	0.968	0.882	0.927
BP	0.868	0.916	0.912	0.976	0.859	0.912
GA-BP	0.863	0.915	0.912	0.975	0.863	0.912

20

1   The performance of different calibration models for the PM against reference monitor is also evaluated using RMSE, MSE and

2   MAE. The results are listed in Table 3, Table 4, and Table 5, respectively. Using the data listed in Table 3, the RMSE values from

3   the first (I) and third (III) periods are large than the one from the second (II) stage, the main reason maybe the large fluctuation

4   range of the PM for the climatic factors in winter and spring resulting in the poor model fit. The RMSE values of $PM_{2.5}$ between

5   the reference data and the RF, MLR, KNN, BP, GA-BP-based algorithms data are within 2.36 - 5.49, 12.63 - 18.68, 5.67 - 13.05,

6   6.56 - 14.35, 6.61 - 14.35, respectively. The RMSE values of PM_{10} between the reference data and the RF, MLR, KNN, BP, GA-

7   BP-based algorithms data are calculated as 4.55 -10.37, 16.43 - 45.05, 11.14 - 27.08, 12.15 - 23.10, and 11.99 - 23.65, respectively.

9   **Table 3. Performance of different calibration models for the $PM_{2.5}$ and PM_{10} against reference monitor. The RMSE values (lower is better)**
10 **of different calibration models (RF, MLR, KNN, BP, GA-BP) versus reference monitor.**

RMSE Model	$PM_{2.5}$			PM_{10}		
	I	II	III	I	II	III
RF	**4.03**	**2.36**	**5.49**	**10.37**	**4.55**	**7.19**
MLR	17.18	12.63	18.68	45.05	16.43	25.22
KNN	9.73	5.67	13.05	27.08	11.14	17.29
BP	11.09	6.56	14.35	23.10	12.15	18.88
GA-BP	11.27	6.61	14.35	23.65	11.99	18.87

12 Using the data listed in Table 4, the MAE values have the same characteristics with RMSE. The MAE values of $PM_{2.5}$ between

13 the reference data and the RF, MLR, KNN, BP, GA-BP-based algorithms data are within 1.44 -3.45, 8.37 - 12.80, 3.56 - 8.31,

14 4.46 - 9.55, and 4.48 - 9.54, respectively. The MAE values of PM_{10} between the reference data and the RF, MLR, KNN, BP, GA-

15 BP-based algorithms data are within 3.21 - 5.28, 12.21 - 23.20, 8.00 - 13.35, 8.99 - 15.26, and 8.89 - 15.43, respectively.

17 **Table 4. Performance of different calibration models for the $PM_{2.5}$ and PM_{10} against reference monitor. The MAE values (lower is better)**
18 **of different calibration models (RF, MLR, KNN, BP, GA-BP) versus reference monitor.**

MAE Model	$PM_{2.5}$			PM_{10}		
	I	II	III	I	II	III
RF	**2.19**	**1.44**	**3.45**	**5.28**	**3.21**	**5.13**
MLR	10.92	8.37	12.80	23.20	12.21	19.10
KNN	5.55	3.56	8.31	13.35	8.00	12.31
BP	7.34	4.46	9.55	15.26	8.99	14.06
GA-BP	7.42	4.48	9.54	15.43	8.89	14.07

4.3 Measurement results of gas pollution

21 With the results from 1 March 2021 to 28 February 2022 and according the trend of the ambient temperature, shown in Figure 9,

22 the whole data is also divided into three same segments as section 4.2. With the same purpose of avoiding over-fit in the five

23 models and ensure the robustness of the model evaluation, the random partition parameters of train ratio and test ratio are also 80%

24 and 20%, and the 5-fold cross validation is also conducted. The time series data and regressions of five modes for gas pollution

25 from reference monitor and LCS calibration output are shown in Figure 12 - Figure 15.
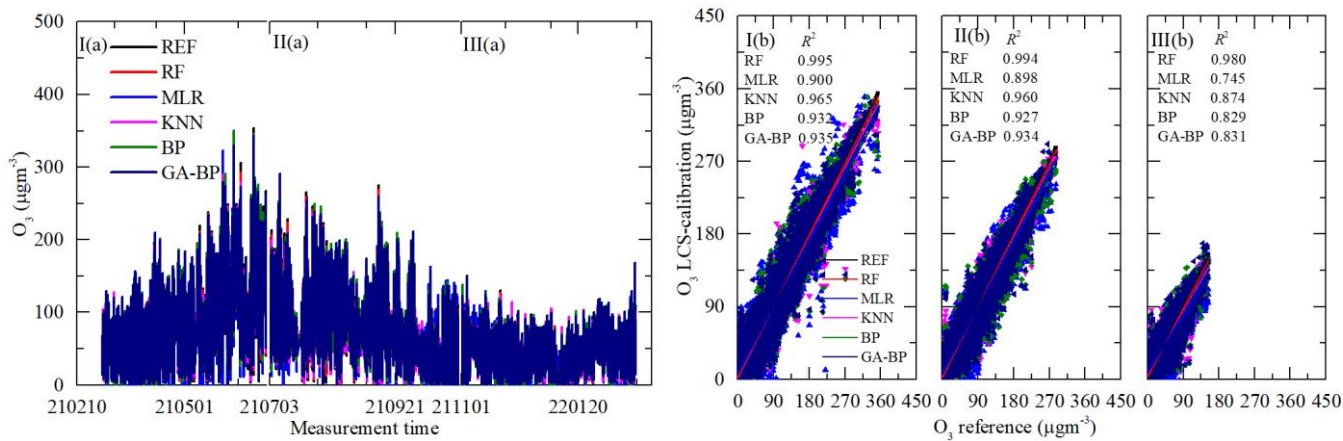
Figure 12. Time series and regressions comparing the reference monitor O₃ data (black) to five calibration model O₃ results. Where red, blue, magenta, olive and navy represent RF, MLR, KNN, BP, GA-BP, respectively. The left panel (a) shows the whole time series data of the measurement period. The right panel (b) shows the regressions of the five calibration models.
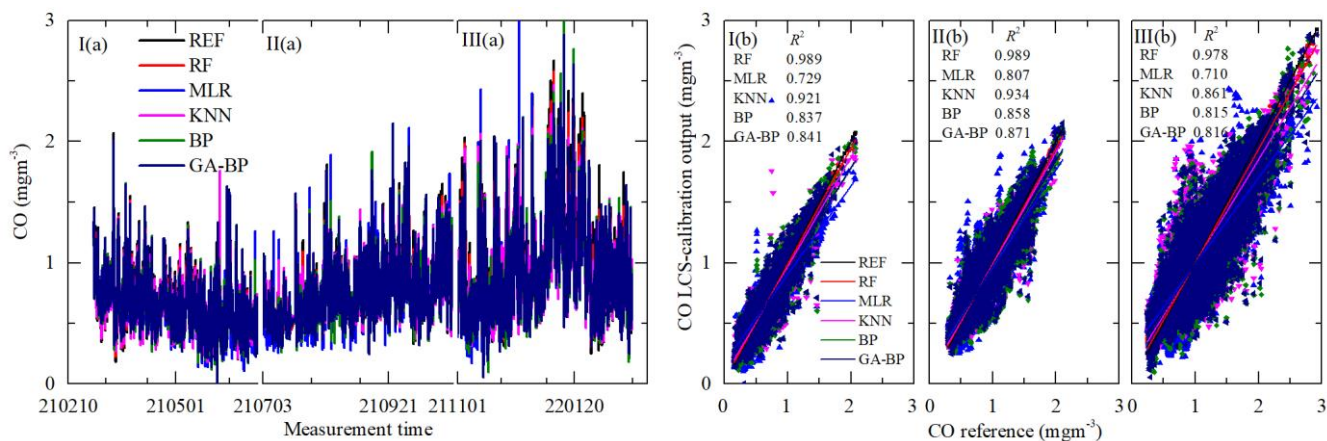
Figure 13. Time series and regressions comparing the reference monitor CO data (black) to five calibration model CO results. Where red, blue, magenta, olive and navy represent RF, MLR, KNN, BP, GA-BP, respectively. The left panel (a) shows the whole time series data of the measurement period. The right panel (b) shows the regressions of the five calibration models.
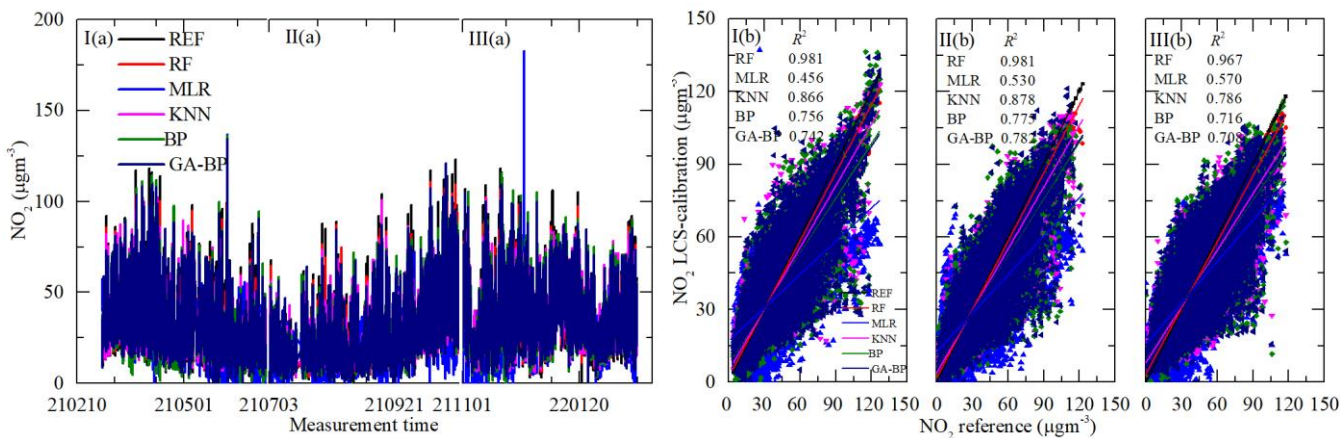
Figure 14. Time series and regressions comparing the reference monitor NO₂ data (black) to five calibration model NO₂ results. Where red, blue, magenta, olive and navy represent RF, MLR, KNN, BP, GA-BP, respectively. The left panel (a) shows the whole time series data of the measurement period. The right panel (b) shows the regressions of the five calibration models.
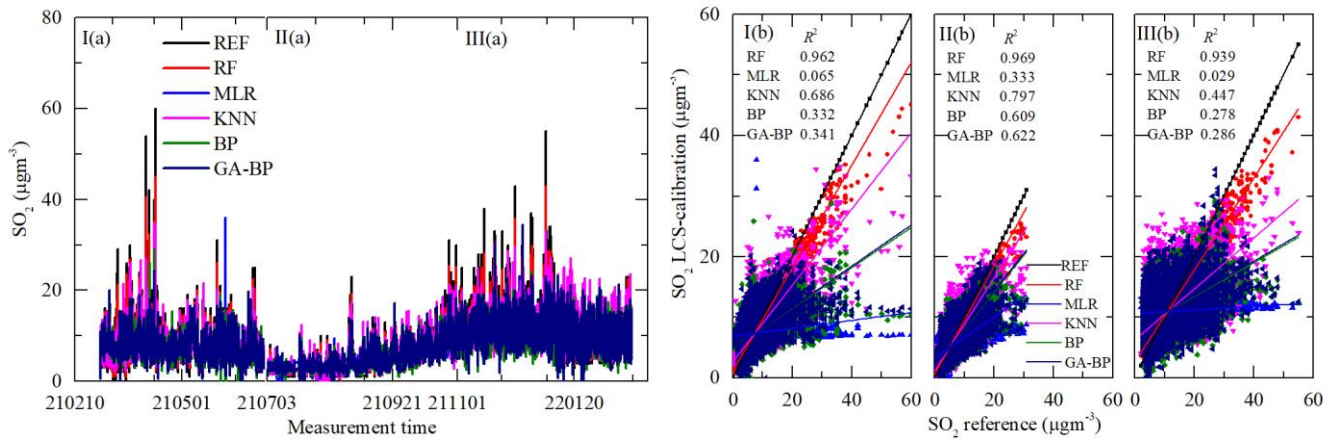
2 **Figure 15. Time series and regressions comparing the reference monitor SO₂ data (black) to five calibration model SO₂ results. Where**
3 **red, blue, magenta, olive and navy represent RF, MLR, KNN, BP, GA-BP, respectively. The left panel (a) shows the whole time series**
4 **data of the measurement period. The right panel (b) shows the regressions of the five calibration models.**

6 As shown in Figure 12(a) - Figure 15(a), the general tendency of the data fluctuation between the reference monitor and the RF,

7 MLR, KNN, BP, GA-BP based algorithm of the LCS are consistent with each other. The best performance is RF model, the next

8 are KNN, BP and GA-BP, the worst is MLR. The R^2 between the reference data and the five model data are also shown in Figure

9 12(b) - Figure 15(b), and listed in Table 5.

10 **Table 5. Performance of different calibration models for the gaseous pollutant (SO₂, CO, NO₂, and O3) against reference monitor. The**
11 **determination coefficient R^2 (higher is better, maximum of 1) of different calibration models (RF, MLR, KNN, BP, GA-BP) versus**
12 **reference monitor.**

R^2 / Model	O_3			CO			NO_2			SO_2		
	I	II	III	I	II	III	I	II	III	I	II	III
RF	**0.995**	**0.994**	**0.980**	**0.989**	**0.989**	**0.978**	**0.981**	**0.981**	**0.967**	**0.962**	**0.969**	**0.939**
MLR	0.900	0.898	0.745	0.729	0.807	0.710	0.456	0.530	0.570	0.065	0.333	0.029
KNN	0.965	0.960	0.874	0.921	0.934	0.861	0.866	0.878	0.786	0.686	0.797	0.447
BP	0.932	0.927	0.829	0.837	0.858	0.815	0.756	0.775	0.716	0.332	0.609	0.278
GA-BP	0.935	0.934	0.831	0.841	0.871	0.816	0.742	0.782	0.708	0.341	0.622	0.286

14 For the O_3 model, the R^2 of RF is better than 0.98. The R^2 of MLR is less than 0.90, and even less than 0.8. The R^2 of the other

15 three models are within 0.82 and 0.97. For the CO model, the R^2 of RF is better than 0.97. The R^2 of MLR is less than 0.81, and

16 even less than 0.7. The R^2 of other three models are within 0.81 and 0.94. For the NO_2 model, the R^2 of RF is better than 0.96. The

17 R^2 of MLR is less than 0.60, and even less than 0.5. The R^2 of other three models are within 0.70 and 0.90. For the SO_2 model, the

18 R^2 of RF is better than 0.93. The R^2 of MLR is less than 0.40, and even less than 0.1. The R^2 of other three models are within 0.27

19 and 0.80.

20 The performances of different calibration models for the gas pollution against reference monitor are also evaluated using RMSE

21 and MAE. The results are listed in Table 6 and Table 7, respectively.

22 **Table 6. Performance of different calibration models for the gaseous pollutant (SO₂, CO, NO₂ and O3) against reference monitor. The**
23 **RMSE values (lower is better) of different calibration models (RF, MLR, KNN, BP, GA-BP) versus reference monitor.**

RMSE / Model	O_3			CO			NO_2			SO_2		
	I	II	III	I	II	III	I	II	III	I	II	III
RF	**4.05**	**4.06**	**4.08**	**0.02**	**0.03**	**0.06**	**2.88**	**2.88**	**3.99**	**0.83**	**0.64**	**1.68**
MLR	17.79	16.42	14.00	0.12	0.12	0.23	14.54	13.54	13.61	3.53	2.69	5.37
KNN	10.57	10.28	9.84	0.06	0.07	0.16	7.25	6.93	9.61	2.06	1.49	4.05
BP	14.67	13.91	11.46	0.09	0.10	0.18	9.75	9.37	11.07	2.98	2.06	4.63
GA-BP	14.40	13.19	11.41	0.09	0.10	0.18	10.02	9.21	11.21	2.97	2.03	4.60

24

Using the data listed in Table 6, the RMSE values of O_3, CO and NO_2 from the first (I) and third (III) periods have little difference with the one from the second (II) period, indicating the O_3, CO and NO_2 electrochemical sensor suitable for the ambient O_3, CO and NO_2 measurement. The RMSE values of O_3 between the reference data and the RF, MLR, KNN, BP, GA-BP-based algorithms data are within 4.05 - 4.08, 14.00 - 17.79, 9.84 - 10.57, 11.46 - 14.67, and 11.41 - 14.40, respectively. The RMSE values of CO between the reference data and the RF, MLR, KNN, BP, GA-BP-based algorithms data are within 0.02 - 0.06, 0.12 - 0.23, 0.06 - 0.16, 0.09 - 0.18, and 0.09 - 0.18, respectively. The RMSE values of NO_2 between the reference data and the RF, MLR, KNN, BP, GA-BP-based algorithms data are within 2.88 - 3.99, 13.54 - 14.54, 6.93 - 9.61, 9.37 - 11.07, and 9.21 - 11.21, respectively.

Using the RF model, the RMSE values of SO_2 are better than the values of other methods, but still have difference during the three periods. However, using other models, the RMSE values of SO_2 from the first (I) and third (III) periods are larger than the one from the second (II) period, the main reason maybe the large ambient fluctuation for the climatic factors in winter and spring, resulting in the poor model fit. The RMSE values of SO_2 between the reference data and the RF, MLR, KNN, BP, GA-BP-based algorithms data are within 0.64 - 1.68, 2.69 - 5.37, 1.49 - 4.05, 2.06 - 4.63, and 2.03 - 4.60, respectively.

Using the data listed in Table 7, the MAE values have the same characteristics with RMSE. The MAE values of O_3 between the reference data and the RF, MLR, KNN, BP, GA-BP-based algorithms data are within 2.76 -2.88, 10.79 - 13.46, 7.06 - 7.33, 8.70 - 11.14, and 8.67 - 10.90, respectively. The MAE values of CO between the reference data and the RF, MLR, KNN, BP, GA-BP-based algorithms data are within 0.02 - 0.05, 0.09 - 0.19, 0.04 - 0.11, 0.07 - 0.14, and 0.07 - 0.14, respectively. The MAE values of NO_2 between the reference data and the RF, MLR, KNN, BP, GA-BP-based algorithms data are within 1.84 - 2.80, 10.41 - 11.08, 4.45 - 6.85, 6.59 - 8.27, and 6.48 - 8.41, respectively. The MAE values of SO_2 between the reference data and the RF, MLR, KNN, BP, GA-BP-based algorithms data are within 0.39 - 1.16, 1.96 - 4.24, 0.91 - 2.84, 1.41 - 3.43, and 1.36 - 3.40, respectively.

Table 7. Performance of different calibration models for the gaseous pollutant (SO_2, CO, NO_2 and O_3) against reference monitor. The MAE values (lower is better) of different calibration models (RF, MLR, KNN, BP, GA-BP) versus reference monitor.

MAE Model	O_3			CO			NO_2			SO_2		
	I	II	III	I	II	III	I	II	III	I	II	III
RF	**2.76**	**2.83**	**2.88**	**0.02**	**0.02**	**0.05**	**1.86**	**1.84**	**2.80**	**0.49**	**0.39**	**1.16**
MLR	13.46	12.77	10.79	0.09	0.09	0.19	11.08	10.41	10.74	2.54	1.96	4.24
KNN	7.33	7.22	7.06	0.04	0.04	0.11	4.74	4.45	6.85	1.25	0.91	2.84
BP	11.14	10.60	8.70	0.07	0.08	0.14	7.07	6.59	8.27	2.08	1.41	3.43
GA-BP	10.90	10.02	8.67	0.07	0.07	0.14	7.31	6.48	8.41	2.05	1.36	3.40

As shown in Figure 12 - Figure 15 and listed in Table 5 - Table 7, the results of each model have little difference among the three periods for the O_3, CO and NO_2 measurement, and the RF model outperforms other models.

For the data of SO_2, the results of RF are better than the ones of other methods, and have little difference among the three periods. However, the performances of other methods (MLR, KNN, BP, GA-BP) are poorer than the one during the first and third periods. There may be some reasons for this phenomenon. The first one is the cross interference effect from NO_2 and O_3, which have the wide range of fluctuations (from about 20 μgm^{-3} to 125 μgm^{-3}) and increasing tendency in period I, respectively. The NO_2 and SO_2 can react chemically under certain conditions to produce sulfuric acid (H_2SO_4) and nitric acid (HNO_3), which will affect the reading of SO_2 sensor. The O_3, highly oxidizing gas, may react with SO_2 to form H_2SO_4 or sulfite (H_2SO_3), resulting in inaccurate sensor readings. The second one is the ambient temperature has a wide range of fluctuations (from about minus 5 ℃ to plus 45 ℃) during the first and third periods, which will affect the stability of electrode material and the readings of the sensor. The last one is the concentration of ambient SO_2 is high (more than 30 μgm^{-3}) in period I and period III, beyond the actual measurement range of the SO_2 sensor, which will be researched in future.

5 Conclusions and Discussion

A low-cost air quality monitoring system (LCS) based on RF, MLR, KNN, BP, GA-BP algorithms are proposed. The system can measure gas-phase pollutants (SO_2, NO_2, CO and O_3) and particle pollutants ($PM_{2.5}$ and PM_{10}), simultaneously. With the purpose to estimate the performance of the five algorithms, the LCS was mounted at the same location (Zhengzhou City, China) and consistent height with the reference monitoring system. The measurement was made continuously from 1 March 2021 to 28 February 2022, with the ranges of the ambient temperature and relative humidity separately minus 5℃ to plus 50℃ and 10% to 98%, respectively. The values of the LCS and reference instruments were separately logged to the server for further comparative analysis.

With the pretreated and individual particle counters, T and RH as input, and the concentrations of $PM_{2.5}$ and PM_{10} measured by the reference instrumentation separately as output, the multi-input one-output evaluation models based on RF, MLR, KNN, BP, GA-BP algorithms can be obtained. With the four types of electro-chemical sensors raw data, T and RH as input, and the measurements from the reference monitors as output, the multi-input multi-output evaluation models based on the five algorithms can be obtained. The performance of the calibration models are quantitatively compared by utilizing R^2, RMSE and MAE.

The experimental results show that the R^2 of RF for the PM is better than 0.98; the R^2 of MLR for the PM is less than 0.91; the R^2 of the other three model are within 0.86 and 0.98. The R^2 of RF for the gas pollutants (SO_2, NO_2, CO and O_3) is better than 0.93; the R^2 of KNN, BP and GA-BP for the gas pollutants (SO_2, NO_2, CO and O_3) is within 0.27 to 0.97; the R^2 of MLR for the NO_2, CO and O_3 is within 0.46 to 0.90, but for SO2 less than 0.40, and even less than 0.1.

The maximum RMSE values of $PM_{2.5}$, PM_{10}, O_3, CO, NO_2, and SO_2 between the reference data and the RF, MLR, KNN, BP, GA-BP-based algorithms data are 5.49, 18.68, 13.05, 14.35, and 14.35; 10.37, 45.05, 27.08, 23.10, and 23.65; 4.08, 17.79, 10.57, 14.67, and 14.40; 0.06, 0.23, 0.16, 0.18, and 0.18; 3.99, 14.54, 9.61, 11.07, and 11.21; 1.68, 5.37, 4.05, 4.63, and 4.60, respectively. The maximum MAE values of $PM_{2.5}$, PM_{10}, O_3, CO, NO_2, and SO_2 between the reference data and the RF, MLR, KNN, BP, GA-BP-based algorithms data are 3.45, 12.80, 8.31, 9.55, and 9.54; 5.28, 23.20, 13.35, 15.26, and 15.43; 2.88, 13.46, 7.33, 11.14, and 10.90; 0.05, 0.19, 0.11, 0.14, and 0.14; 2.80, 11.08, 6.85, 8.27, and 8.41; 1.16, 4.24, 2.84, 3.43, and 3.40, respectively.

It is should be noted that the results of RF are better than the ones of other methods, have very good agreement with the reference monitors and little difference among the three periods. However, the performances of other methods (MLR, KNN, BP, GA-BP) have poor agreement, especially during the first and third periods. There may be some reasons, such as the cross interference effect, the wide range of fluctuation of the climatic factors, and the limitation of the actual measurement range and precision.

Overall, we conclude that, with careful data management and calibration using the machine learning algorithms, especially the RF method, these measurements are consistent with the national environmental protection standard requirement of China, the LCS may significantly improve our ability to spatial heterogeneity in air pollutant concentrations. The air pollutant maps will assist researchers, policymakers, and communities in developing new policies or mitigation strategies to enhance human health. In the next research, we will focus on improving the matching of the measurement precise and range, the generalization of the algorithms in more applications, and the performance of the SO_2 sensor.

Competing interests

The contact author has declared that none of the authors has any competing interests.

Acknowledgment

Funding for this study was provided by the National Key Research and Development Program of China (Assistance Agreement No. 2021YFB3200403) and Zhengzhou Education Department (No. 23B413006). The authors also wish to thank Minghui, Li, Hongbiao Liu, and Jinlong Wang for helpful conversations.

References

Alexopoulos, E. C.: Inroduction to Multivariate Regression Analysis. Hippokratia, 14(1), 23-28, https://www.ncbi.nlm.nih.gov/pmc/articles/PMC3049417/, 2010.

Ali, S., Glass, T., Parr, B., Potgieter, J., and Alam, F.: Low Cost Sensor With IoT LoRaWAN Connectivity and Machine Learning-Based Calibration for Air Pollution Monitoring. IEEE Transactions on Instrumentation and Measurement, 70, 5500511, https://doi.org/10.1109/TIM.2020.3034109, 2021.

Amuthadevi, C., Vijayan, D. S., and Ramachandran, V.: Development of air quality monitoring (AQM) models using different machine learning approaches. Journal of Ambient Intelligence and Humanized Computing, 33(2022), https://doi.org/10.1007/s12652-020-02724-2, 2021.

Breiman, L.: Random Forests. Machine Learning, 45(1), 5-32, https://doi.org/10.1023/A:1010933404324, 2001.

Chai, T., and Draxler, R. R.: Root mean square error (RMSE) or mean absolute error (MAE)? - Arguments against avoiding RMSE in the literature. Geoscientific Model Development, 7(1525-1534), https://doi.org/10.5194/gmd-7-1247-2014, 2014.

Chew, C. G., Latifah, M. K., Ammar, Z., Hiromitsu, N., Nuraminah, R., Mao, X., Syed, M., Ericson, K., Abdul, S., and Md., F.: Real-Time In-Vehicle Air Quality Monitoring System Using Machine Learning Prediction Algorithm. Sensors, 21, 4956, https://doi.org/10.3390/s21154956, 2021.

China, M. o. E. a. E. o. t. P. s. R. o. (2018). Technical specifications for operation and quality control of ambient air quality continuous automated monitoring system for SO2, NO2, O3 and CO. In (Vol. HJ 818-2018).

China, M. o. E. a. E. o. t. P. s. R. o. (2020). Technical guide for automatic monitoring by beta ray method for particulate matter in ambient air (PM_{10} and $PM_{2.5}$). In (Vol. HJ 1100).

Cross, E. S., Williams, L. R., Lewis, D. K., Magoon, G. R., Onasch, T. B., Kaminsky, M. L., and Worsnop, D. R.: Use of electrochemical sensors for measurement of air pollution: correcting interference response and validating measurements. atmos. Meas. Tech., 10(9), 3575-3588, https://doi.org/10.5194/amt-10-3575-2017, 2017.

Cui, H., Zhang, L., Li, W., Yuan, Z., Wu, M., Wang, C., and Ma, J.: A new calibration system for low-cost Sensor Network in air pollution monitoring. Atmospheric Pollution Research, 12(5), 101049, https://doi.org/10.1016/j.apr.2021.03.012, 2021.

Davut, A., and Baykant, A. B.: An effective integrated genetic programming and neural network model for electronic nose calibration of air pollution monitoring application. Neural Computing and Applications, 34(15), 12633-12652, https://doi.org/10.1007/s00521-022-07129-0, 2022.

Esposito, E., De, V. S., Salvato, M., Bright, V., Jones, R. L., and Popoola, O.: Dynamic neural network architectures for on field stochastic calibration of indicative low cost air quality sensing systems. Sensors Actuators B-Chemical, 231, 701-713, https://doi.org/10.1016/j.snb.2016.03.038, 2016.

Hande, B., and Selda, G.: Estimation of Concentration Values of Different Gases Based on Long Short-Term Memory by Using Electronic Nose Biomedical Signal Processing and Control, 69, https://doi.org/10.1016/j.bspc.2021.102908, 2021.

Hitchman, M. L., Cade, N. J., Gibbs, T. K., and Hedley, N. J. M.: Study of the factors affecting Mass Transport in Electrochemical Gas Sensors. Analyst, 122(11), 1411-1417, https://doi.org/10.1039/a703644b, 1997.

Ionascu, M. E., Castell, N., Boncalo, O., Schneider, P., Darie, M., and Marcu, M.: Calibration of CO, NO_2, and O_3 Using Airify: A Low-Cost Sensor Cluster for Air Quality Monitoring. Sensors, 21(23), 7997, https://doi.org/10.3390/s21237977, 2021.

Janabi, S. A., Alkaim, A., Al-Janabi, E., Aljeboree, A., and Mustafa, M.: Intelligent forecaster of concentrations ($PM_{2.5}$, PM_{10}, NO_2, CO, O_3, SO_2) caused air pollution (IFCsAP). Neural Computing and Applications, 33(21), 14199-14229, https://doi.org/10.1007/s00521-021-06067-7, 2021.

Khreis, H., Johnson, J., Jack, K., Dadashova, B., and Park, E. S.: Evaluating the Performance of Low-Cost Air Quality Monitors in Dallas, Texas. International Journal of Environmental Research and Public Health, 19(3), 1647, https://doi.org/10.3390/ijerph19031647, 2022.

Kumar, T.: Solution of Linear and Non Linear Regression Problem by K Nearest Neighbour Approach: By Using Three Sigma Rule. 2015 IEEE International Conference on Computational Intelligence & Communication Technology, 197-201, https://doi.org/10.1109/CICT.2015.110, 2015.

Liang, Y., Ren, C., Wang, H., Huang, Y., and Zheng, Z.: Research on soil moisture inversion method based on GA-BP neural network model. International Journal of Remote Sensing, 40(5-6), 2087-2103, https://doi.org/10.1080/01431161.2018.1484961, 2018.

Liu, Y., Wang, Y., and Zhang, J.: New machine learning algorithm: Random forest. Information Computing and Applications. Proceedings of the Third International Conference, ICICA 2012, 7473, 246-252, https://doi.org/10.1007/978-3-642-34062-8_32, 2012.

Mahesh, T. R., Vinoth, K. V., Dhilip, K. V., Oana, G., Martin, M., and Manisha, G.: The stratified K-folds cross-validation and class-balancing mehtods with high-performance ensemble classifiers for breast cancer classification. Healthcare Analytics, 2023, 100247, https://doi.org/10.1016/j.health.2023.100247, 2023.

Manisalidis, I., Stavropoulou, E., Stavropoulos, A., and Bezirtzoglou, E.: Environmental and Health Impacts of Air Pollution: A Review. Frontiers in Public Health, 8(14), 1-13, https://doi.org/10.3389/fpubh.2020.00014, 2020.

Masson, N., Piedrahita, R., and Hannigan, M.: Quantification method for electrolytic sensors in long-term monitoring of ambient air quality. Sensors, 15(10), 27283-27302, https://doi.org/10.3390/s151027283, 2015.

Mead, M. I., Popoola, O. A. M., Stewart, G. B., and Landshoff, P.: The use of electro-chemical sensors for monitoring urban air quality in Low-cost, high-density networks. Atmos. Environ., 70, 186-203, https://doi.org/10.1016/J.ATMOSENV.2012.11.060, 2013.

Ning, M., Guan, J., Liu, P., Zhang, Z., and O'Hare, G. M. P.: GA-BP Air Quality Evaluation Method Based on Fuzzy Theory. CMC-Computers Materials & Continua, 58(1), 215-227, https://doi.org/10.32604/cmc.2019.03763, 2019.

Reza, R., Behzad, N., and Gulen, G.: A Comparative study of Deep Learning Models on Tropospheric Ozone Forecasting Using Feature Engineering Approach. Atmosphere, 14, 239, https://doi.org/10.3390/admos14020239, 2023.

Singh, A., Ng'ang'a, D., Gatari, M. J., Kidane, A. W., Alemu, Z. A., Derrick, N., and Webster, M. J.: Air quality assessment in three East African cities using calibrated low-cost sensors with a focus on road-based hotspots. Environmental Research Communications, 3(7), 075007, https://doi.org/10.1088/2515-7620/ac0e0a, 2021.

Spinelle, L., Gerboles, M., Villani, M. G., Aleixandre, M., and Bonavitacola, F.: Field calibration of a cluster of low-cost available sensors for air quality monitoring. Part A: Ozone and nitrogen dioxide. Sensors Actuators, B Chem., 215, 249-257, https://doi.org/10.1016/j.snb.2015.03.031, 2015.

Spinelle, L., Gerboles, M., Villani, M. G., Aleixandre, M., and Bonavitacola, F.: Field calibration of a cluster of low-cost commercially available sensors for air quality monitoring. Part B: NO, CO and CO_2. Sensors and Actuators B-Chemical, 238, 706-715, https://doi.org/10.1016/j.snb.2016.07.036, 2017.

Wan, J., Gayle, H., Ronald, W., Robert, S., Ryan, B., Daniel, G., and Robert, J.: Community Air Sensor Network (CAIRSENSE) project: evaluation of low-cost sensor performance in a suburban environment in the southeastern United States. atmos. Meas. Tech., 9(11), 5281-5292, https://doi.org/10.5194/amt-9-5281-2016, 2016.

Wang, C., Pan, B., Wu, X., Song, Y., Zhang, L., Ma, J., and Sun, K.: Research on Quality Control of Atmospheric Grid Monitoring Based on Large Data Analysis. Environmental Monitoring in China 32(6), 1-6, https://doi.org/10.19316/j.issn.1002-6002.2016.06.01, 2016.

Wang, S., Li, L., Ma, W., and Chen, X.: Trajectory analysis for on-demand services: A survey focusing on spatial-temporal demand and supply patterns. Transportation Research Part C: Emerging Technologies, 108, 74-99, https://doi.org/10.1016/j.trc.2019.09.007, 2019.

Wei, P., Ning, Z., Ye, S., Sun, L., and Yang, F.: Impact Analysis of Temperature and Humidity Conditions on Electrochemical Sensor Response in Ambient Air Quality Monitoring. Sensors, 18(2), https://doi.org/10.3390/s18020059, 2018.

Xu, X., Guo, H., and Fan, J.: Water quality evaluation of Xiaoshan water quality station in eastern Zhejiang Water Diversion Project Based on BP network. Journal of Physics: Conference Series, 1732, 012035, https://doi.org/10.1088/1742-6596/1732/1/012035, 2021.

Zhao, C., Wang, Y., Shi, X., Zhang, D., Wang, C., Jiang, J., and Zhang, Q.: Estimating the Contribution of Local Primary Emissionsto Particulate Pollution Using High‐Density Station Observations. J. Geophys. Res.: Atmospheres, 124, 1648-1661, https://doi.org/10.1029/2018JD028888, 2019.

Zhao, P., and Lai, L.: Minimax Rate Optimal Adaptive Nearest Neighbor Classification and Regression. IEEE Transactions on Information Theory, 67(5), 3155-3182, https://doi.org/10.48550/arXiv.1910.10513, 2021.

Zhu, N., Zhu, C., Zhou, L., Zhu, Y., and Zhang, X.: Optiminzation of the Random Forest Hyperparameters for Power Industrial Control Systems Intrusion Detection Using an Improved Grid Search Algorithm. Applied Sciences, 12, 10456, https://doi.org/10.3390/app122010456, 2022.

Zimmerman, N., Presto, A. A., Kumar, S. P. N., Gu, J., Hauryliuk, A., Robinson, E. S., and Robinson, A. L.: A machine learning calibration model using random forests to improve sensor performance for lower-cost air quality monitoring. atmos. Meas. Tech., 11(1), 291-313, https://doi.org/10.5194/amt-11-291-2018, 2018.

Zoest, V. v., Osei, F. B., Stein, A., and Hoek, G.: Calibration of low-cost NO_2 sensors in an urban air quality network. Atmospheric Environment, 210, 66-75, https://doi.org/10.1016/j.atmosenv.2019.04.048, 2019.